Graphite Felt-Sandwiched Ni/SiC Catalysts for the Induction Versus Joule-Heated Sabatier Reaction: Assessing the Catalyst Temperature at the Nanoscale

Lai Truong-Phuoc, Cuong Duong-Viet, Giulia Tuci, Andrea Rossin, Jean-Mario Nhut, Walid Baaziz, Ovidiu Ersen, Mehdi Arab, Alex Jourdan, Giuliano Giambastiani, et al.

Graphite Felt-Sandwiched Ni/SiC Catalysts for the Induction *vs*. Joule-Heated Sabatier Reaction: Assessing the Catalyst Temperature at the Nanoscale

Lai Truong-Phuoc,[a,] Cuong Duong-Viet,[a,] Giulia Tuci,[b] Andrea Rossin,[b]*

Jean-Mario Nhut,[a] Walid Baaziz,[c] Ovidiu Ersen,[c] Mehdi Arab,[d] Alex Jourdan,[d]

Giuliano Giambastiani,[a,b,] Cuong Pham-Huu[a]**

[a] *Institute of Chemistry and Processes for Energy, Environment and Health (ICPEES), ECPM, UMR 7515 of the CNRS and University of Strasbourg, 25 rue Becquerel, 67087 Strasbourg Cedex 02, France. Email: ltruongphuoc@unistra.fr, giambastiani@unistra.fr and cuong.pham-huu@unistra.fr*

[b] *Institute of Chemistry of OrganoMetallic Compounds, ICCOM-CNR and Consorzio INSTM, Via Madonna del Piano, 10, 50019 Sesto F.no, Florence, Italy. Email: giuliano.giambastiani@iccom.cnr.it*

[c] *Institute of Physic and Chemistry of Materials of Strasbourg (IPCMS), UMR 7504 CNRS-University of Strasbourg,23 rue du Loess, 67037 Strasbourg Cedex 08, France*

[d] *ORANO Tricastin, Direction de La Recherche & Développement, Site du TRICASTIN BP 16, 26701 Pierrelatte Cedex*

Abstract

The paper describes a series of graphite felt (GF)-sandwiched ^{k}Ni/SiC composites at variable metal loading (k = 10, 15 and 20 wt.%) and their application as catalysts for the CO_2 methanation process (Sabatier reaction) under two distinct and conceptually different heating setup: *Joule heating vs*. *Induction heating*. A comparative analysis carried out on all catalysts from this series operated under the two heating configurations, has unveiled the superior performance of radiofrequency heated (IH) catalysts in the process. Most importantly, it has offered a practical tool to map the gap existing between the macroscopic temperature value measured at the catalyst bed by a remote-sensing thermometer (pyrometer) and that (real) of the excited metal nano-objects (Ni NPs) directly engaged in the radiofrequency-heated catalytic process. Besides the evident advantages of IH technology applied to the methanation process in terms of process rates (λ) already under nominally low-reaction temperatures, the virtual absence of any thermal inertia and the subsequent fast modulation of the temperature at the catalytic bed, demonstrate unique features of this heating technology in terms of process safety (cold-reactor walls) and reduction of energy wastes (neither pre- and post-catalyst heating of reagents and products, nor that of the whole reactor volume and its peripheral walls).

Keywords: Induction heating; Methanation reaction; Joule Heating; Temperature of inductively heated nano-objects; SiC-based catalysts.

Introduction

The development of integrated chemical strategies for the energy conversion and storage is a key priority of our modern society to address a truly renewable energy-based transition.[1] In the Power-to-Gas (P2G) chain, the exceeding amount of electrical energy produced from renewable and CO_2-free energy suppliers (*i.e.* wind, hydraulic, solar) is converted into H_2 *via* water electrolysis. If not immediately used, H_2 can be employed as reagent in the CO_2 hydrogenation (Sabatier or methanation process)[2-5] to give substitute natural gas (SNG; CH_4). SNG is an energy vector of more practical use/management/distribution within the existing infrastructures and gas-grids. Storage and transport conditions for methane are also easier and cheaper compared to those required for hydrogen.

CO_2 methanation is a highly exothermic process (ΔH^0 = -165 kJ mol^{-1}); nevertheless, it requires the use of catalysts along with large external heat input to overcome the severe kinetic limitations linked to CO_2 chemical inertness.[6] External heating implies larger energy costs burdening on the process. In addition, its combination with the reaction exothermicity and the thermal inertia of classically Joule-heated (JH) reactors hampers an accurate temperature control at the catalytic bed where local temperature gradients (*hot-spots*) can be formed. The latter are typical sources of serious drawbacks and technical limitations linked to the catalyst stability and its performance on long term runs other than represent a primary energy waste for the process.

In recent years, new achievements in catalysis have mainly pointed out on the process intensification[7] by guarantee a quantum leap in its efficiency in terms of time, energy costs, employ of non-critical raw materials and environmental impact rather than squeezing few percentages on the yield and selectivity of consolidated protocols of the *state-of-the-art*. The electromagnetic induction heating (IH) or radiofrequency (RF) heating of electrically conductive or magnetic susceptors has already been exploited for a wide range of targeted

applications, spanning from biomedical area[8-9] in the treatment of diseases (through magnetic hyperthermia)[10] to that of processes for metallurgic manufacturing.[11] Only recently, this technology has been exploited in catalysis[12] spotting light on the unique potentiality of this "non-contact" technology for the heat management in highly exo- and endothermic processes.[12] The possibility to convey heat only where it is needed for the chemical process using magnetic or electrically conductive susceptors/catalysts has been used to overcome several heat transfer limitations occurring in classical (Joule) heating schemes. IH indeed limits energy wastes associated to undesired and detrimental heating paths[12-13] and drastically reduces the thermal inertia (heating/cooling rate) at the catalytic bed.[12]

As far as CO_2 methanation reaction is concerned, IH has successfully been exploited by means of magnetic nanoparticles (NPs) and/or core-shell systems joining high hyperthermic efficiency[14-16] to excellent catalytic performance. Similarly, electrically conductive susceptors decorated with catalytically active NPs have been employed as robust catalytic systems to run CO_2 hydrogenation under severe and dynamic conditions.[12] We have recently described a RF-heated methanation scheme based on highly Ni-loaded/γ-Al_2O_3 (up to 40 wt.%) composites as electrically conductive and magnetic susceptor/catalysts for a rational heat management at the catalytic bed and with a drastic reduction of the nominal temperature values needed to perform efficiently the process [CO_2 conversion (X_{CO2}) up to 98% with methane selectivity (S_{CH4}) > 99% already at operative temperatures of 210-230 °C].[13] Evidences from this study have led us to conclude that the catalyst temperature measured at the catalytic bed by a remote-sensing thermometer (pyrometer; ∅ laser beam: ≈ 500 μm, power < 1mW) is an average value between that of the support (γ-Al_2O_3) and that of the radiofrequency excited nickel particles decorating its surface (catalytic sites). These results, together with others related from the literature,[17-18] support the idea of a temperature gap between the value measured by the laser spot (macroscopic) and that (*real*) of the heated nano-objects (Ni NPs).

Anyhow, the precise determination of the entity of this gap and thus the temperature value at the nanoscale remains a challenging task to be addressed,[14, 19-21] particularly in continuous flow, fixed-bed reactors operated under relatively harsh experimental conditions. Current technologies applied to this challenging task are generally based on the development and use of thermo-sensitive molecules as molecular temperature probes[19] as well as advanced spectroscopic techniques as diagnostic tools for the determination of the local temperature values.[21]

This paper describes the design and synthesis of a new family of graphite felt (GF)-sandwiched ^{k}Ni/SiC composites with variable metal loading (k = 10, 15 and 20 wt.%) as catalysts/susceptors for the methanation process to be operated under two distinct heating technologies: *Joule heating vs. Induction heating*. The choice of nickel as metal active sites is based on its renewed catalytic activity and stability in the process. Moreover, its magnetic properties make it a useful susceptor to run the process under IH conditions. SiC is a semiconductor, non-oxide ceramic featured by good thermal conductivity but not suitable to convert electromagnetic energy into heat (not radiofrequency heatable).[22] To improve the hyperthermic efficiency of the catalytic system, Ni/SiC was sandwiched between two electrically conductive and IH-responsive (eddy or Foucault currents) graphite-felt disks. The comparative analysis of these catalytic materials under different heating configuration (JH *vs.* IH) and experimental conditions (reaction temperature, *gas-hourly-space-velocity* - GHSV) has provided a practical tool for mapping the temperature gap existing between the macroscopic value measured at the catalyst bed by the pyrometer and that (*real*) of the excited metal nano-objects (Ni NPs) directly engaged in the radiofrequency-heated catalytic process.

At the same time, the catalytic study under IH has pointed out the superior performance of catalysts operated with this direct and non-contact heating technology together with its key advantages in terms of process safety (cold-reactor walls) and reduction of energy wastes.

Experimental Section

Materials and Methods

Silicon carbide (SiC) was purchased from Sicat SARL (www.sicatcatalyst.com) as mesoporous pellets (3 x 1 mm, h x Ø)[23-25] with a specific surface area (SSA) measured by N_2 physisorption (at 77 K) of 27 ± 3 m^2 g^{-1}. SiC pellets were thoroughly washed with distilled water and oven dried for several hours at 140 °C to remove all powdery fractions prior to be employed as supports for the preparation of the Ni-based composites. Unless otherwise stated, all other reagents and solvents were used as received by the providers without any specific purification/treatment.

Synthesis of ^{k}Ni/SiC composites. In a typical procedure, SiC pellets (8 g) were impregnated with a proper amount (3.0, 4.8 and 6.8 mL) of a 5 M aqueous $Ni(NO_3)_2 \cdot 6H_2O$ solution to get ^{k}Ni/SiC with a theoretical metal charge of k = 10, 15 and 20 wt.%, respectively. Impregnated samples were evaporated and oven dried at 110 °C for 2 h before being calcined in air at 350 °C for 2 h as to prepare the corresponding metal oxides. The as obtained ^{k}NiO/SiC pre-catalysts (k = 10, 15 and 20 wt.%) underwent reduction treatment under a pure H_2 flow (100 mL min^{-1}) at 350 °C for 2 h. This reduction step was accomplished as an *in-situ* pre-catalyst treatment whatever the nature of heating setup [Joule heating (JH) or Induction heating (IH)] employed for the CO_2 methanation trials. *Scanning Electron Microscopy* (SEM) was carried out on a ZEISS 2600F instrument with a resolution of 5 nm. 10 kV electron beam was used for SEM imaging operated in high vacuum mode, using BSE and SE detectors. For measurements, samples were deposited onto a double face graphite tape holder as to avoid charging effect during the analysis. *Transmission electron microscopy* (TEM) was carried out on a JEOL 2100F working at 200 kV accelerated voltage, equipped

with a probe corrector for spherical aberrations, and a point-to-point resolution of 0.2 nm. Elemental mapping was finally accomplished by *Scanning Transmission Electron Microscopy* (STEM) on a JEOL 2100F electron microscope equipped with a Gatan Energy Filter and cold field-emission gun (FEG) operated at 200 kV with 1.5Å lattice resolution. For these measurements, samples were dispersed by ultrasounds treatment (5 min) in an ethanol solution and a drop of each suspension was deposited on a copper grid covered with a holey carbon membrane for observation. *Powder X-ray diffraction* (PXRD) measurements were carried out on a D8 Advance Bruker diffractometer with a Cu Kα X-ray source (λ = 1.5406 Å). Rietveld refinements are performed by GSAS-II software.[26] The mean size of ordered (crystalline) domains (τ) is calculated from the Debye-Scherrer equation: $\tau = K\lambda/\beta\cos\theta$, where K is a shape factor, λ is the X-ray wavelength, β is the line broadening at half the maximum intensity (FWHM) and θ is the Bragg angle. The Brunauer-Emmett-Teller (BET) *Specific Surface Areas* (SSA) were calculated from N_2 physisorption isotherms recorded at 77 K on an ASAP 2020 Micromeritics® instrument. Pore Size Distribution was determined by Barrett-Joyner-Halenda (BJH) method applied to the desorption isotherm branches. Each sample was degassed/activated at 250 °C under vacuum for 8 h in order to desorb moisture and adsorbed species on its surface. *Thermogravimetric analyses* (TGA) were run under air (100 mL min^{-1}) on a TGA Q5000 thermogravimetric analyser (TG/DTA) using a heating rate of 10 °C/min. The average weight measured for each sample was maintained around 10 mg maximum. *Inductively-Coupled Plasma Optical Emission Spectrophotometry* (ICP-OES) measurements on mineralized ^{k}NiO/SiC pre-catalysts were accomplished on a Varian 720 ES ICP-OES instrument. The induction heating setup (EasyHeat® 8310, 4.2kW, Ambrell Ltd) is made of a 6-turn spiral induction coil (length = 1.05 m, pure coil resistance = 2.066 x 10^{-3} Ω), cooled by means of an external chiller containing a water/glycerol (10 %, v/v) as cooling mixture. For the temperature measurement in a typical radiofrequency heated (IH) experiment, temperature

at the catalyst bed was monitored/controlled/regulated in almost real-time by a PID system (Proportional Integral Derivative controller, Eurotherm model 3504) connected to a laser pyrometer (Optris®, ø laser beam: ≈ 500 μm, power < 1mW, located at ≈ 15 cm from the catalyst and working in the 150-1000 °C range with an accuracy ± 1°C), shot up on the catalyst/susceptor. A standard calibration procedure[27] has been used to fix the emissivity factor for each ^{k}Ni/SiC (k = 10, 15, 20 wt.%) catalyst of the study. The heating/cooling rate allowed for the system was about 60-80 °C min^{-1} in the 150-300 °C temperature range. The inductor frequency was constantly maintained at 265 ± 5 kHz while the current flowing the induction coils varied from 200 A to 450 A.

Induction Heating setup. In a typical experiment, the quartz reactor containing the catalyst was housed inside the coils of the induction heater and temperature real-time control/regulation was ensured by a PID system (Proportional Integral Derivative controller, Eurotherm model 3504) connected to a laser pyrometer (remote-sensing thermometer) shot up on the catalyst bed (see Figure 3 for the sake of clarity).

Joule Heating setup (electrical oven). In a typical experiment, the quartz reactor containing the catalyst was housed in an electrical oven (ERALY Co., $\varnothing_{OD}$ = 200 mm; $\varnothing_{ID}$ = 55 mm; depth: 300 mm; I_{max} = 8.6 A, T_{max} = 1100 °C). The temperature of the system was monitored by two type-K thermocouples, one for regulating the oven temperature (T_F) and an additional one located in close contact with the catalytic bed (T_C) for measuring the temperature swings throughout the process. For these trials, we used thermocouples of $\varnothing_{ED.}$ 0.5 mm, very close to the dimension of the laser pyrometer spot in IH. Before each catalytic run, catalyst was allowed to reach and stabilize (30-45 min) at the target temperature under a pure stream of He (max temperature deviation recorded between T_F (F = furnace) and T_C (C = catalyst) after stabilization = ± 3 °C) (see Figure 3 for the sake of clarity).

Catalytic tests. CO_2 methanation reaction (Eq. 1) was conducted at atmospheric pressure in a fixed-bed quartz tubular reactor [$Ø_{ID}$ = 12 mm, length = 400 mm] charged with 0.6 g of ^{k}Ni/SiC catalyst (k = 10, 15 and 20 wt.%; V ≈ 0.8 cm^3) and housed on the proper heating setup (EasyHeat® 8310 induction heating setup or a classical external furnace).

$$CO_2 + 4\,H_2 \rightarrow CH_4 + 2\,H_2O \quad \Delta H = -165\ kJ\ mol^{-1} \qquad \text{(Eq. 1)}$$

In a typical catalytic run, a H_2/CO_2 gas mixture (4 v/v) at variable *GHSV*s obtained by a series of calibrated Mass Flow Controllers (Brookhorst®) was continuously fed through the catalytic bed maintained at the target temperature. Gases at the reactor outlet are passed through a trap filled with silicon carbide pellets where water is condensed before reaching the gas chromatograph for analysis. Reactants and products were analysed on-line at the respective reactor outlets by a R3000 (SRA Instrument) micro gas chromatograph (μGC) equipped a MS5A column for H_2, CH_4, CO detection and a PPU column for CO_2, C_2 detection with thermal conductivity (TCD). All reactors exit lines were maintained at 110 °C by external heating tapes as to avoid water condensation in the feed.

CO_2 conversion (X_{CO2}) and CH_4 selectivity (S_{CH4}) were calculated according to the following equations (Eqs. 2 and 3):

$$X_{CO_2}(\%) = \frac{F_{CO_2(in)} - F_{CO_2(out)}}{F_{CO_2(in)}} x100 \qquad \text{(Eq. 2)}$$

$$S_{CH_4}(\%) = \frac{F_{CH_4(out)}}{F_{CH_4(out)} + F_{CO(out)}} x100 \qquad \text{(Eq. 3)}$$

… where $F_{i(in/out)}$ (mL min^{-1}) is the flow rate of each component in the gas feed at the reactor inlet or outlet.

Results and Discussion

Synthesis and characterization of ^{k}Ni/SiC catalysts (k = 10, 15 and 20 wt.%)

^{k}Ni/SiC composites (k = 10, 15 or 20 wt.%) were straightforwardly prepared by wet impregnation (WI) technique followed by conventional thermal calcination/reduction steps (see Experimental Section for procedure details). The impregnated solids were oven dried at 110 °C for 2 h and calcined in air at 350 °C for additional 2 h as to convert the nickel nitrate into its corresponding oxide. Catalysts were further reduced under a hydrogen flow (100 mL/min) at 350 °C for 2 h. All composites from this series were thoroughly characterized by PXRD, TEM/STEM and N_2-physisorption analyses while their effective metal loading was determined (on NiO pre-catalysts) through ICP-OES measurements.

The catalysts composition and the average Ni NPs size before and after the NiO reduction were systematically analysed through PXRD. Figure 1 shows the PXRD patterns recorded for the three ^{k}Ni/SiC (k = 10, 15 and 20 wt.%) samples at comparison with the model system ^{10}NiO/SiC, arbitrarily selected as a representative pre-catalytic system from this series. Hydrogenation (H_2 flow: 100 mL/min, at 350 °C for 2 h) of all calcinated pre-catalysts provides a complete NiO conversion into the corresponding Ni^0 particles. NiO diffraction peaks (at 2θ = 37.3, 43.4, 63.0, 75.6 and 79.6° respectively)[28] are almost quantitatively suppressed in all reduced samples while new distinctive peaks ascribed to Ni^0 appear at 2θ = 44.5, 51.8 and 76.3°.[29] Expectedly, the peak intensity of the latter grows up appreciably when passing from 10 to 20 wt.% of metal loading in the SiC normalized spectra. Notably, the chemical inertness of the SiC carrier is likely at the origin of the pure Ni^0 phases obtained in all samples after the reduction step. The absence of strong chemical interactions between the metallic phase and the non-oxide ceramic support is witnessed by the absence of hardly reducible forms[22] at the interface, resistant to the relatively mild reduction conditions used. The Ni particle size was roughly estimated using the Scherrer equation[30] applied to the peak full width at half maximum (FWHM) of diffraction peaks at 2θ = 44.5 and 51.8°. The mean

values measured for the ^{k}Ni/SiC samples were fixed to 13 ± 1, 21 ± 2 and 26 ± 2 nm for k = 10, 15 and 20 wt.%, respectively.

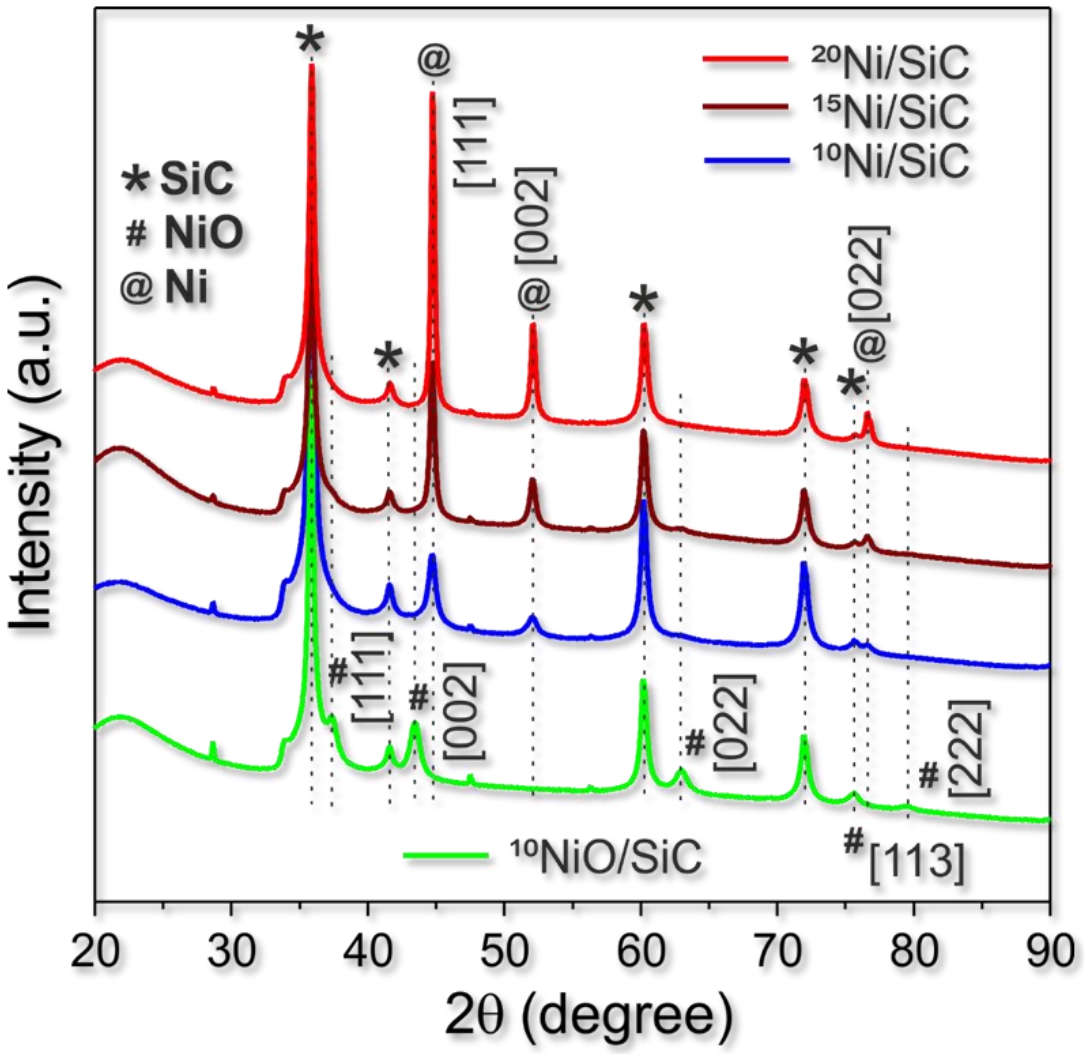

Figure 1. PXRD profiles of ^{10}NiO/SiC and ^{k}Ni/SiC (k = 10, 15 and 20 wt.%) at comparison.

The higher the metal loading the higher the mean nickel particle size and the generation of larger metal aggregates. While Ni/SiC composites at relatively low Ni contents (*i.e.* ^{10}Ni/SiC) can boast a higher stability extent due to the presence of amorphous SiO_2/SiO_xC_y layers at the carrier topmost surface that contribute to stabilize and disperse the metal active phase,[22, 31] higher metal loadings and larger metal aggregates on supports with moderate SSA are less leaching-resistant. As an example, SEM images of the ^{20}Ni/SiC catalyst (Figure S1) at

different magnifications unveil the almost complete coating of the SiC carrier with nickel superstructures and structural vacancies; the latter are probably originated by a partial removal of poorly stabilized nickel aggregates. Therefore, the higher the metal content used in the catalysts' preparation the higher the deviation between the theoretical and the effective metal loading in the composites. This trend was confirmed by the ICP-OES analysis on the final catalysts. While ^{10}Ni/SiC sample showed an excellent match between the theoretical and the measured nickel loading (9.3 ± 0.3 wt.%), ^{20}Ni/SiC displayed the higher deviation from the theoretical content (17.0 ± 0.8 wt.%) (Table 1). At odds with XRD data, XPS surface analyses of all Ni/SiC composites unveiled the presence of NiO_x forms (Figure S2A and B)[32] resulting from a rapid passivation of metal deposits during the samples handling in air and their manipulation for analysis (formation of thin metal-oxide layers). For this reason, each NiO/SiC pre-catalyst underwent H_2 flow reduction at 350 °C *in situ* (see experimental section) just prior of its exposure to the reagents' mixture for catalysis. The specific surface area (SSA), the total pore volume and the mean pore size measured for all Ni-composites (Table 1, entries 2-4 and Figure S3B-D) were very similar and close to the morphological parameters recorded for bare SiC support (Table 1, entry 1 and Figure S3A). All samples present classical Type II isothermal profiles and moderate specific surface area values. The meso-macroporous nature of the ceramic carrier was moderately affected by the deposition of Ni NPs and by the final metal loading in the composite. Although any conclusion based on these moderate morphological deviations remains speculative and poorly significant to the manuscript purposes, it can be simply claimed that the higher the metal charge, the lower the SSA value of the composite.

Table 1. ICP-OES analysis, specific surface area (SSA), pore volume and pore size distribution measured on each ^{k}Ni/SiC (k = 10, 15 and 20 wt.%) composite at comparison with the bare ceramic support.

Entry	Sample	Ni wt.%	SSA[a]	Total pore	Average

		(ICP-OES)	($m^2 g^{-1}$)	volume [b] ($cm^3 g^{-1}$)	pore size [c] (nm)
1	SiC	-	27	0.16	23.8
2	^{10}Ni/SiC	9.3 ± 0.3	29	0.14	17.6
3	^{15}Ni/SiC	14.0 ± 0.5	26	0.13	21.6
4	^{20}Ni/SiC	17.0 ± 0.8	24	0.13	22.6

[a] Brunauer-Emmett-Teller (BET) specific surface area (SSA) measured at T = 77 K. [b] Total pore volume determined using the adsorption branch of N_2 isotherm at P/P_0 = 0.98. [c] Determined by BJH desorption average pore width (4V/A).

Transmission Electron Microscopy on ^{k}Ni/SiC (Figures 2A-B for k = 10 and Figures 2D-E for k = 15 wt.%) showed a relatively homogeneous dispersion of metal nanoparticles all over the SiC support. Moreover, a statistical analysis of NPs size distribution carried out on each catalyst (Figures 2C and 2F) was in good agreement with PXRD outcomes. HRTEM analysis (Figure S4) on ^{10}Ni/SiC has finally revealed the presence of crystalline phases featured by distinctive interplanar distances of 0.21 and 0.24 nm, characteristic of the (1 1 1) planes of Ni[33] and SiC[34] phases, respectively.

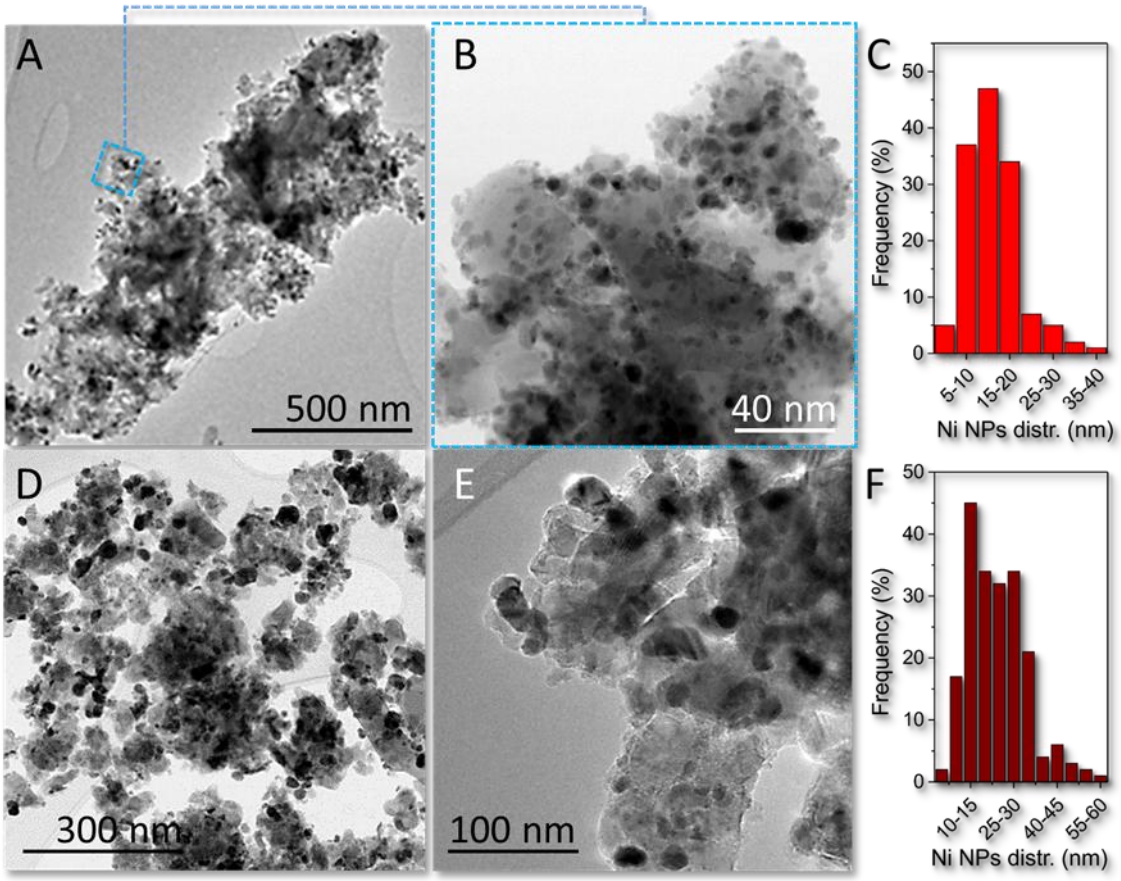

Figure 2. TEM images recorded on ^{10}Ni/SiC (A-B) and ^{15}Ni/SiC (D-E) at different magnifications along with the statistical distribution of NPs sizes determined over 100 metal particles for each sample. C and F refer to the Ni NPs size distribution on ^{10}Ni/SiC and ^{15}Ni/SiC, respectively.

3.2 *Methanation reaction with ^{k}Ni/SiC as catalyst under two heating configurations: Joule-heating vs. Induction-heating.*

Looking for more efficient and energy saving approaches to methanation reaction, the ^{k}Ni/SiC (k = 10, 15 and 20 wt.%) catalysts were investigated under two different reactor configurations: i) a classical reactor scheme (Figure 3A) using an electrical furnace for the catalyst heating through convection, conduction and/or radiation heat transfer (named hereafter as *Joule-heating* mode; JH) or ii) an induction heating setup (Figure 3C) based on the electro-magnetic properties of a susceptible medium (susceptor) exposed to a varying

magnetic field (H) and its ability to convert the electromagnetic energy into heat at the catalytic bed or neighboring it (named hereafter as *induction-heating* mode; IH).

For both reactors, temperature values were registered at the respective macroscopic heating sources. Therefore, for JH system (Figure 3A) the temperature was monitored by two thermocouples housed in the furnace (temperature of the furnace, T_F) and in close contact with the quartz reactor (temperature of the catalyst, T_C), respectively. For the radiofrequency heated setup (Figure 3C), the temperature was measured by a remote-sensing thermometer (pyrometer) with its laser beam directly shot over the graphite felt (GF) susceptor (see Experimental section and § "*On the origin of ΔT values[…]*" for details).

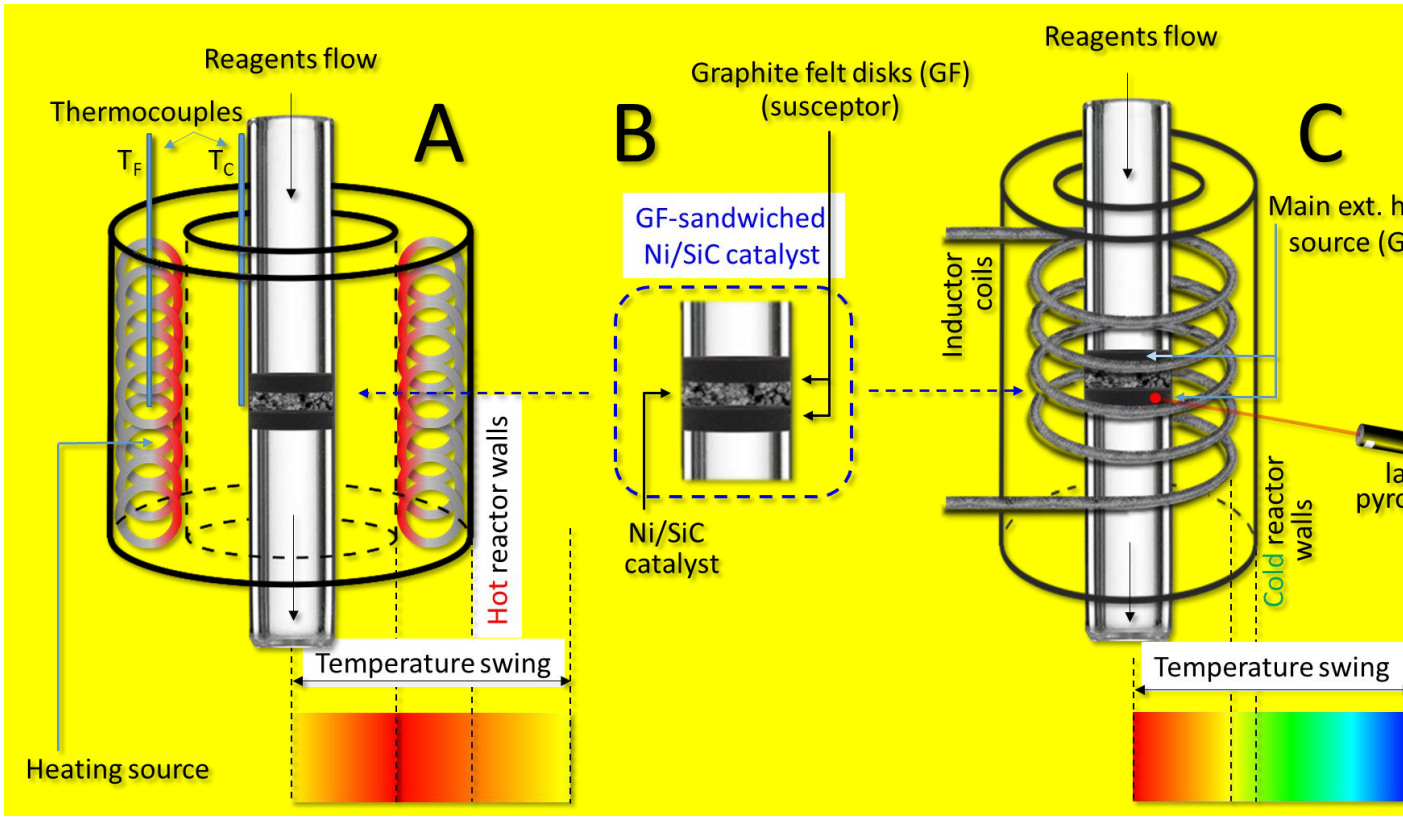

Figure 3. Representation of the adopted reactor configurations to carry out the methanation process; A) Electrical furnace (hot-wall reactor) operating with a classical Joule heating scheme based on heat convection, conduction and radiation; B) Details of the ^{k}Ni/SiC catalyst sandwiched between two graphite-felt disks (susceptors) and housed in the quartz tube reactor; C) Inductor coil for the radiofrequency heating of a susceptible medium (GF, susceptor) exposed to an external varying magnetic field (H). Thermal spectra reported below each reactor configuration, account for the classical temperature diffusion (to and from the catalyst) depending on the operating heating technology (JH or contact and IH or contactless).

Whatever the heating configuration employed, ^{k}Ni/SiC powders were sandwiched in the quartz reactor between two GF disks (Figure 3B). The latter were innocent, porous and thermal conductor supports for the catalytic material when the reaction was operated under JH configuration (Figure 3A) whereas they assumed the role of susceptors for the electromagnetic energy conversion into heat when the reaction was carried out under IH (Figure 3C; see also § "*On the origin of ΔT values[…]*" for details). Blank tests carried out using the GF alone did not show any CO_2 methanation activity in the range of operational temperatures.

Effect of the reaction temperature and heat management setup (JH vs. IH) on the methanation performance.

In a first set of experiments, we studied the effect of the reaction temperature at the catalyst bed on its performance using both heating configurations (JH *vs.* IH) while maintaining constant the amount of catalyst (600 mg) and the reagents *gas-hourly-space-velocity* (GHSV; 10,000 mL g^{-1} h^{-1}). As Figure 4 shows, catalysis under JH (- ●-) presented classical sigmoidal trends for CO_2 (X_{CO2}) conversion into synthetic natural gas (SNG) whatever the catalytic system at work (^{k}Ni/SiC, k = 10, 15 and 20 wt.%). Although ^{10}Ni/SiC reached the higher CO_2 conversion (X_{CO2}) at 350 °C (and kept it almost unchanged in the 350-375 °C range), ^{15}Ni/SiC and ^{20}Ni/SiC showed their higher performance at 375 °C. As expected, the higher the nickel loading the higher the X_{CO2} although the specific catalysts rate (λ) expressed as mol_{CH4} produced per g_{Ni} per *h* was superior with ^{10}Ni/SiC (see Table S1).

Under these operative temperatures (< 400 °C) and irrespective of the employed heating setup, the SNG process selectivity laid constantly close to 100% with no traces of CO or other

by-products detected at the reactors' outlet. The remarkably high S_{CH4} was partially due to the thermal conductivity of the SiC carrier[22] that was thought to mitigate the generation of local temperature gradients (hot-spots) by diffusing extra heat to the whole catalyst volume[35] and ultimately favoring its removal by the action of the gaseous reagents stream (solid-gas heat exchange).

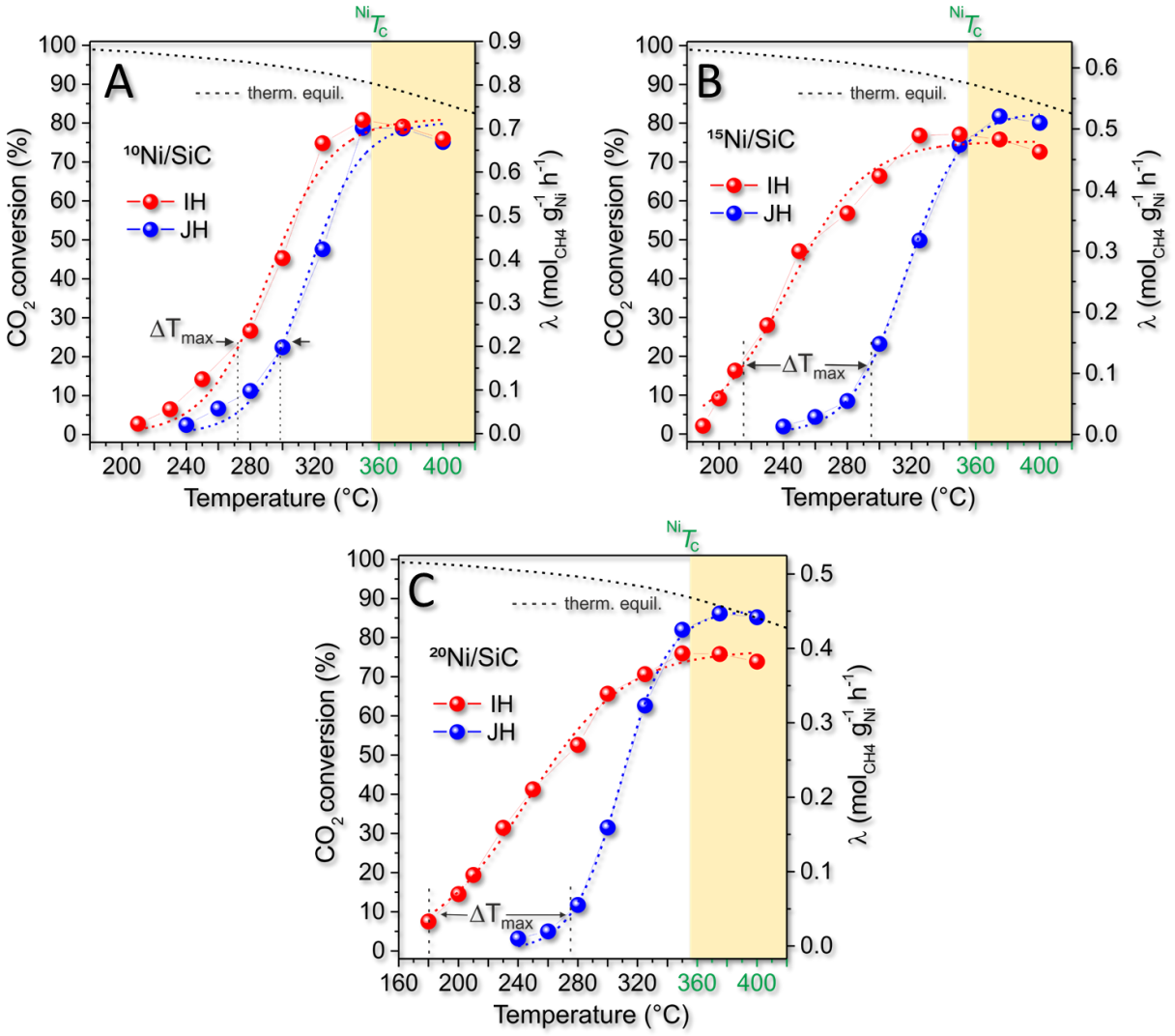

Figure 4. CO_2 methanation with ^{k}Ni/SiC (k = 10 (A), 15 (B) and 20 wt.% (C)) as a function of the reaction temp. All catalysts were tested without any thermic diluent. Reaction conditions: catalyst weight = 600 mg, GHSV (STP) = 10,000 mL g^{-1} h^{-1}, [CO_2] = 20 vol. %, [H_2] = 80 vol. %, H_2-to-CO_2 ratio = 4, total flow rate = 100 mL min^{-1}, atmospheric pressure. Red (- ●-) and blue (- ●-) curves refer to the X_{CO2} *vs*. temperature as experimentally determined within an Induction heating (IH) and Joule-heating (JH) setup, respectively. CH_4 selectivity (S_{CH4}, not shown in figures) was constantly equal to 100 % in the whole temperature range. Thermodynamic equilibrium conversion (dashed black line "-----") has been included for the

sake of comparison. All experimental data have been fitted with sigmoidal logistic functions of type I.

Such a heat exchange was even more efficient in a radiofrequency heated catalyst, because of the absence of reagents flow pre-heating till they came in contact with the (hot) catalyst surface.

When CO_2 methanation was carried out under IH (- ●-), we observed an appreciably higher catalyst performance already for temperatures below 350 °C whatever the metal-loading of the catalyst at work. Remarkably, X_{CO2} measured at 280 and 300 °C with ^{15}Ni/SiC was up to 48 and 43 % higher than that measured under the same experimental conditions but for catalysts operated under JH mode (Figure 4B). As a result, higher productivity values (λ) were recorded for the radiofrequency heated ^{15}Ni/SiC already at nominal low-temperature (280 °C) values (Table S1). This result is of great relevance particularly in light of an industrial exploitation of these catalysts in combination with IH technology. The higher catalyst specific rate (λ) measured at low-reaction temperatures with the radiofrequency heated ^{15}Ni/SiC fulfils at least three key prerequisites of a sustainable methanation scheme: i) catalysts with a relatively low loading of a highly dispersed and non-critical metal active phase; ii) relatively mild operative temperatures to get high X_{CO2} values chemoselectively into SNG; iii) a safer and really energy-saving reactor configuration for the heat management at the catalytic bed.

It should be stressed that Ni-composites at higher metal loading (*i.e.* ^{15}Ni/SiC and ^{20}Ni/SiC) deviate appreciably from the classical sigmoidal profile when catalysis was operated under IH. Such a behaviour was ascribed to a more complex heat management at the catalytic bed in the case of radiofrequency heated catalysts. Indeed, contributions to the catalyst heating derive in part from the inductively heated GF-disks (heat transfer by convection/conduction to the thermally conductive SiC support), in part from dissipation

paths related to the electrically conductive and magnetic nature of the large sized Ni NPs (i.e. eddy currents or Foucault currents and/or heat supplied *via* hysteresis losses).[12] As a proof of evidence, lower X_{CO2} and λ values measured under IH for temperatures higher than 350 °C (Figure 4B-C) can be reasonably attributed to the loss of one heat dissipation path (e.g. heat hysteresis) as a function of the temperature-effect on the metal magnetic properties (*vide infra* § "*On the origin of ΔT values[…]*" for details).[36-37]

Arrhenius plots (Figure 5) constructed as the logarithm of the catalyst process rate [Ln(λ)] *vs*. the reciprocal of the reaction temperature (K^{-1}), have contributed to better distinguish among the catalytic performance of ^{k}Ni/SiC catalysts operated under the two heating setup (Figure 3). Expectedly, when CO_2 methanation was carried out under JH-mode, the three catalysts behave similarly from a kinetic viewpoint, showing almost equal activation energy (curves' slope in Figure 5A and E_a values in Table 2) for processes operated under identical conditions. Moreover, calculated E_a values were in excellent agreement with related literature data for the methanation process.[38-40] Reversely, IH showed important deviations in the curves' slope (Figure 5B), hence implying relevant alterations of the activation energy values associated to the process.

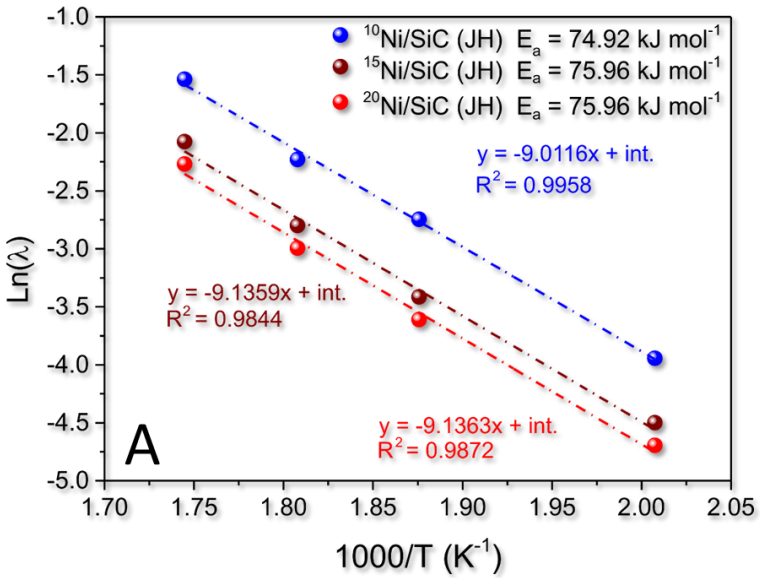

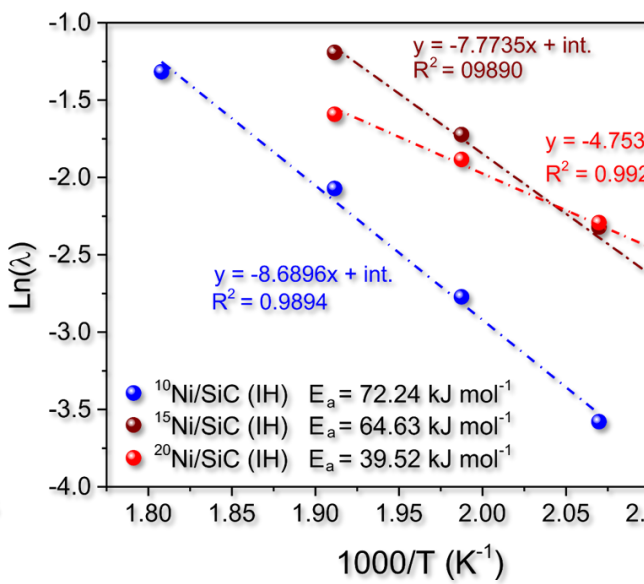

Figure 5. Arrhenius plots of ^{k}Ni/SiC (k = 10, 15 and 20 wt.%) in CO_2 methanation under classical Joule heating (JH; A) or Induction heating (IH; B) setup. λ is expressed as mol_{CH4} g_{Ni}^{-1} h^{-1} and measured in the temperature range where X_{CO2} reaches 30% conversion maximum.

As Table 2 shows, the higher the catalyst metal loading the lower the activation energy (E_a) for the inductively heated methanation process and thus the higher the ΔE_a(JH-IH) gap measured for the reaction operated under different heating configurations.

It is evident that differences in the activation energy values (ΔE_a) measured for the same process, operated with the same catalyst but under different heating schemes (JH vs. IH) had to be ascribed to the existence of a temperature gap between the value measured (macroscopically) at the GF surface and those (real) of the radiofrequency heated nano-objects (nickel active sites) at the SiC surface.

Table 2. Nickel particle size in the three ^{k}Ni/SiC (k = 10, 15 and 20 wt.%) and activation energy values (E_a) calculated for the CO_2 methanation reaction carried out under JH or IH from the respective Arrhenius plots.

Entry	Sample	Ni NPs Ø (nm)[a]	E_a (JH)[b] (kJ mol^{-1})	E_a (IH)[b] (kJ mol^{-1})	ΔE_a (JH-IH) (kJ mol^{-1})	ΔT_{MAX} (°C)[c]	M_s (emu g^{-1})[d]
1	^{10}Ni/SiC	13 ± 1	75.0	72.2	2.8	26 ± 3	47.5 ± 0.7
2	^{15}Ni/SiC	21 ± 2	76.0	64.6	11.4	81 ± 4	51.2 ± 0.6
3	^{20}Ni/SiC	26 ± 2	76.0	39.5	36.5	95 ± 4	52.4 ± 0.4

[a] Determined by XRD from the Scherrer equation and the peak full width at half maximum (FWHM) of the diffraction peaks at 2θ = 44.5 and 51.8°. [b] Calculated from the curves' slopes of Arrhenius plots in the temperature range where X_{CO2} reaches 30% conversion maximum. [c] Determined as the maximum difference on the x-axis (ΔT, °C) of curves in Figures 4AC between two points at the same CO_2 conversion (X_{CO2} on JH and IH curves) as the maximum ΔT value (ΔT_{max}) between the GF-temperature (bulk temperature) and that effectively reached at the excited metal catalyst particles sites. [d] Specific saturation magnetization (M_s) determined for the different Ni particles sizes on the basis of Eq.4 and assuming a mean NiO layer of 0.5 nm in accordance with the TEM analysis on the samples of this study.

Several precedents from the literature have already demonstrated the existence of important temperature discrepancies (up to orders of magnitude)[17] between values reached at the surface of radiofrequency heated nano-objects (metal NPs) and those measured

macroscopically by a remote-sensing thermometer on the bulk materials.[41-44] The temperature measurement at the level of single catalyst particles (especially for magnetically responsive elements) remains a challenging issue to be addressed, and it becomes even more tricky under *operando conditions* in severe experimental environments.[19-21, 45] Anyhow, from the analysis of curves in Figures 4A-C it can be inferred that the maximum difference on the x-axis (ΔT, °C) between two points at the same CO_2 conversion (X_{CO2} on JH and IH curves) corresponds to the maximum ΔT value (ΔT_{max}) between the "macroscopic" temperature measured at the GF-disks and that actually reached at the radiofrequency-excited nickel particles. Accordingly, 26 ± 3 °C, 81 ± 4 °C and 95 ± 4 °C are the ΔT_{max} values between GF and Ni NPs in the RF-heated Ni/SiC catalysts containing 10, 15 and 20 wt.% of metal NPs, respectively.

As expected, such a ΔT value varies as a function of the magnetic properties of Ni NPs, hence their mean particle size as well as the dependence of the nickel specific saturation magnetization (M_s) from the temperature (§ "*On the origin of ΔT values[…]*" for details).

On the origin of ΔT values in radiofrequency heated [k]Ni/SiC catalysts applied to CO_2 methanation reaction

There are no doubts that the two heating configurations (JH and IH) hold distinct thermal and energetic features. Indeed, the radiofrequency heating of a GF-sandwiched catalyst always occurs in a "cold-walls reactor" modality,[20] hence avoiding any pre- and post-heating of reagents and products, including that of the whole reactor volume and its peripheral walls. Such a configuration fosters (among the others) the reaction thermodynamic by favoring H_2O condensation just after the (hot) catalytic bed and reduces all thermal inertia phenomena

typically encountered on furnace-based reactors while guarantying more sustainable and energy saving catalytic schemes.[12]

Similar benefits linked to a more convenient heat management at the catalytic reactor, have recently been commented by others for different gas-phase processes.[46-47]

It is clear that classical heat transfer by conduction/radiation (JH) applies to both heating configurations (JH and IH) proposed in this work. Under IH, the GF-sandwiched catalyst realizes a sort of micro-JH reactor. The thermal dissipation caused by the electromagnetically-induced eddy currents flowing the GF fibers can be considered as the main source of external heating (Figure 3B) for the catalyst active sites *via* classical conduction/radiation heat exchange. As an electrical semiconductor, SiC is not suitable to directly convert electromagnetic energy into heat at the catalytic bed; however, its thermal conductivity conveys the heat produced by the GF disks to the catalyst active sites. Assuming the methanation exothermicity as independent from the nature of the adopted heating setup, under IH the electrically conductive and magnetic nickel deposits (catalyst active phase) undergoes dedicated heating paths.[48] In particular eddy currents (or Foucault currents)[49-50] flowing through the larger metal aggregates and hysteresis loss[51-52] phenomena can induce local heating directly at the metallic phase. Hysteresis loss depends from the specific saturation magnetization (M_s) of the metal particles. It is a key property of ferromagnetic particles and varies as a function of the metal nanoparticles size and their ultimate temperature. Kuz'min demonstrated with a simple analytical representation the shape of the temperature dependence[53] for bulk Ni NPs. He properly described the finite-temperature properties of these ferromagnets in the -273.15 °C - Curie Temperature (T_c, °C; $^{Ni}T_c$ = 355 °C)[54] range, with the latter value corresponding to the temperature where M_s vanishes.[36] Duan and co-workers finally combined the morphological properties (TEM and XRD) of various grain sized Ni NPs prepared by the autocatalytic reduction of a Ni^{II} salt with the M_s size-

dependence. Their study provided a useful model for the calculation of the experimental M_s value for similarly prepared Ni NPs-based catalysts in the form of spontaneously surface-passivated (NiO-coated) systems like ours (see § "*Synthesis and characterization of* ^{k}*Ni/SiC catalysts*" for details). Based on their model (Eq. 4) and assuming a mean size of our Ni NPs of 13, 21 and 26 nm with an average thickness of the NiO thin layer for all catalysts of about 0.5 nm (see also Figure S4B), we calculated M_s values comprised between 47.5 and 52.4 emu/g (see Table 2), in excellent accord with the Ni NPs size/M_s-dependence reported in the literature.

$$M_s^{exp} = \frac{\sigma_s^{bulk} \times {}^4/_3\pi r^3 \times \rho_{Ni}}{{}^4/_3\pi r^3 \times \rho_{Ni} + {}^4/_3\pi (R^3 - r^3)\rho_{NiO}} \qquad \text{(Eq. 4)}$$

… where ρNi = 8.8 g cm^{-3}, ρNiO = 6.827 g cm^{-3}, σ_s^{bulk} = 57.50 emu g^{-1}, R = mean radius of Ni NPs from XRD analysis and r = (R - average thickness of NiO thin layer).

The higher the M_s value, the higher the hyperthermic efficiency or *Specific Absorption Rate* (SAR) of the nickel-based sample and thus the higher its capacity to act as heat susceptor[55] once immerged in an AC magnetic field.[56] The increasing values of ΔT_{max} measured on Ni/SiC samples with variable nickel-loading and nickel particle size (Figures 4A-C) are perfectly in line with these conclusions. Interestingly, JH and IH curves recorded in Figures 4A-C present similar converging trends in close correspondence to the $^{Ni}T_c$ value (355 °C). These trends led us to conclude that the extra-heat (ΔT) generated under IH at the catalytic nickel sites was essentially due to hysteresis loss dissipation phenomena that were definitively suppressed when the metal sites became paramagnetic,[57-58] *i.e.* above $^{Ni}T_c$. Accordingly, it can be concluded that eddy current contributions are almost negligible whatever the nickel loading in the three catalysts at comparison. The moderate or null contribution from eddy currents was finally confirmed by the increasing X_{CO2} conversion gap (or λ gap) measured with the two ^{k}Ni/SiC catalysts at higher metal-loadings (k = 15 and 20

wt.%) operated under JH and IH at temperatures > 355 °C (above $^{Ni}T_c$). Under these conditions, the higher the catalyst particle size the higher the X_{CO2} conversion gap between the two processes. Because eddy currents are directly proportional to the square of the NP radius, then their contribution should follow an opposite trend to that recorded for catalysts ^{15}Ni/SiC and ^{20}Ni/SiC operated in the CO_2 methanation at temperatures > $^{Ni}T_c$.

According to the observed trends of X_{CO2} *vs*. temperature recorded where the Ni NPs become paramagnetic (yellow sections of Figures 4A-C), it can be concluded that catalysts heating occurred through convection/conduction only. For the two RF-heated catalysts at higher Ni-loading (^{15}Ni/SiC and ^{20}Ni/SiC) the reduced catalysts process rates for temperatures > $^{Ni}T_c$ are then ascribed to a less effective Joule heating transfer in the micro-JH reactor (GF-sandwiched catalyst) with respect to the classical external furnace. In contrast with the classical furnace, the formally cold walls of the micro-JH reactor facilitate a more rapid heat dissipation from the catalytic bed. Therefore, it can be inferred that this phenomenon in combination with the suppressed magnetic properties of Ni particles further contributed to the observed decrease of the catalysts' performance.

Effect of the reactants flow rate (GHSV) on the methanation performance of a JH or IH ^{15}Ni/SiC catalyst.

The influence of the reactants space velocity (GHSV) was deliberately investigated on ^{15}Ni/SiC as one of the most representative samples from this catalyst series at the temperature of 300 °C where the ΔX_{CO2} and $\Delta\lambda$ values measured under the two heating configurations (JH and IH) were the highest (Figure 4B and Table S1, entries 15-16). As Figure 6A shows, selectivity towards CH_4 laid constantly over 99% with no detectable traces of any other

reaction byproduct whatever the adopted heating configuration and the gas flow applied to the reactor in the 10-25 L g^{-1} h^{-1} GHSV range.

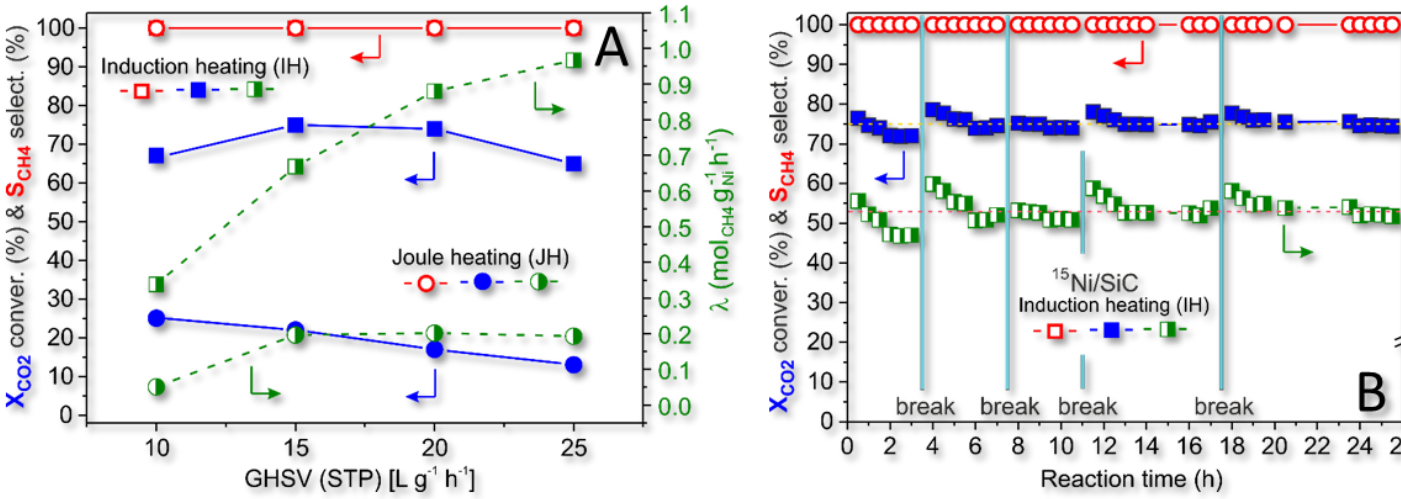

Figure 6. A) X_{CO2} and productivity rate (λ) dependence from the applied GHSV (L g^{-1} h^{-1}) for methanation processes operated on ^{15}Ni/SiC as catalyst under JH (round symbols) and IH (square symbols) mode. B) Long-term methanation test at 20,000 mL g^{-1} h^{-1} as GHSV under discontinuous mode using the inductively heated ^{15}Ni/SiC catalyst. Each break corresponds to the reactor switching-off overnight. Other common reactional conditions for A and B: [CO_2] = 20 vol. %; [H_2] = 80 vol. %; H_2-to-CO_2 ratio = 4; catalyst weight = 0.6 g; reaction temperature = 300 °C, atmospheric pressure.

As far as X_{CO2} and λ values are concerned, the two heating configurations translated into radically different catalyst behaviors. Under JH mode, X_{CO2} decreased for increasing flow rates and catalyst productivity (λ) remained substantially unchanged throughout the last three reagents rates. When the process was operated under IH, an initial X_{CO2} increase was observed and the catalyst productivity grew constantly (and appreciably) for increasing reactants flows. It should be stressed that Δλ in ^{15}Ni/SiC, operated under the two heating schemes (JH and IH) and at increasing reactants flow rates (from 10,000 to 25,000 as GHSV), increased over 190 % (Table S1, entries 15-16 vs. 21-22). There were little doubts that different values and trends in X_{CO2} measured within the two heating configurations at increasing GHSVs, reflected a radically different control of the temperature at the catalytic

bed of the two reactors. All X_{CO2} decreasing trends measured at increasing GHSVs can be claimed as the consequence of several factors such as: i) an oversaturation of the metal active sites; ii) a reduced contact time of reagents with the catalyst active phase and iii) a reduced catalyst temperature due to a more effective solid-gas heat exchange at increasing reactants flow rates. All these phenomena may contribute to reducing X_{CO2} when GHSVs increases. However, *i* and *ii* items certainly do not justify the growing trend of X_{CO2} measured under IH when the reaction was operated between 10,000 and 15,000 GHSVs. In contrast to classical JH reactors, temperature swings at the catalytic bed caused by growing flow rates (warming) and increased solid-gas heat exchanges (cooling) are rapidly controlled and compensated (with almost no thermal inertia) by a fast modulation of the current flowing the inductor coils (remote-sensing thermometer connected to the inductor through a PID controller).

This excellent catalyst temperature control is also at the origin of a prolonged stability and durability of inductively heated catalysts on methanation run. Figure 6B refers to a long-term methanation test operated with the radiofrequency heated ^{15}Ni/SiC catalyst at 300 °C with 20,000 mL g^{-1} h^{-1} as GHSV and in a discontinuous process (successive reactor shut-downs; breaks) as to add a further stress factor to the long catalytic trial (> 25 h). As it can be seen, after an initial stabilization the catalyst constantly laid on an average X_{CO2} = 75 ± 2% with a quantitative methane selectivity and a productivity (λ) that closely approached 0.9 mol_{CH4} g_{Ni}^{-1} h^{-1}.

The combination of the IH-setup with the inherent thermal conductivity of SiC supports reduces all classical drawbacks associated to catalysts deactivation on run. TEM analysis of the catalytic material before and after the long-term run, has demonstrated the superior stability of the catalytic system once operated under IH. Indeed, neither relevant changes in the nanoparticles size distribution (sintering) nor appreciable catalyst coking phenomena after long-term runs were revealed (Figure S5 and S6).

Conclusions

In summary, we compared ^{k}Ni/SiC composites at variable metal loading as catalysts for the Sabatier process under two different heating configurations (JH vs. IH). The study has unambiguously demonstrated the superior performance, stability and durability of catalysts operated under the less conventional IH setup. The superior performance of radiofrequency heated catalysts (already at relatively low temperatures) basically stems from a different heat management at the catalytic bed. The comparative analysis between the two heating schemes along with the study of process kinetics have offered a practical and simple tool to the estimation of the temperature gap between that measured directly at the main heat source and that (real) of the radiofrequency heated nano-objects (metal NPs). If we assume any catalyst heating/cooling contributions (i.e. reaction exothermicity; solid-gas heat exchanges at varying GHSVs; heat dissipation by SiC support) as equal regardless the nature of the heating configuration at work (IH and JH), such a temperature difference is unambiguously associated to the distinctive heat dissipation properties (eddy currents and hysteresis loss) of the electrically conductive and magnetic nickel particles immersed in the AC magnetic field.

Besides the evident benefits of IH technology applied to the methanation process in terms of X_{CO2} and process rates (λ) already under nominally low-reaction temperatures, the virtual absence of thermal inertia phenomena and the subsequent fast modulation of the temperature directly at the catalytic bed, hold unique advantages in terms of process safety (cold-reactor walls) and reduction of energy wastes (neither pre- and post-catalyst heating of reagents and products, nor that of the whole reactor volume and its peripheral walls). Finally, the choice of silicon carbide as support for the metal active phase has guaranteed a better temperature control at the catalytic bed. Indeed, SiC thermal conductivity allows the bidirectional heat

transfer between the GF disks (susceptors under IH) and the Ni NPs, avoiding the formation of local hot spots that reduce process selectivity and the catalyst lifetime.

Acknowledgements

The present work was supported by ORANO Co. through a contract No. 40104671. G. G. and C. P.-H. would like to thank the TRAINER project (Catalysts for Transition to Renewable Energy Future) of the "Make our Planet Great Again" program (Ref. ANR-17-MPGA-0017) for support. G. G. and G. T. would also like to thank the Italian MIUR through the PRIN 2017Project Multi-e (20179337R7) "Multielectron transfer for the conversion of small molecules: an enabling technology for the chemical use of renewable energy" for financial support to this work. The silicon carbide material was supplied by SICAT SARL (www.sicatcatalyst.com) and Dr. Ch. Pham is gratefully acknowledged for helpful discussion. The SEM analysis was carried out at the joint SEM platform of the ICPEES-IPCMS and T. Romero (ICPEES) is gratefully acknowledged for performing the experiments.

Supporting Information. SEM, HRTEM, BET and pore-size distribution (BJH) of ^{k}Ni/SiC (k = 10, 15, 20 wt.%); XPS survey and Ni $2p_{3/2}$ of ^{15}Ni/SiC; X_{CO2} and catalyst specific rate (λ) for CO_2 methanation with ^{k}Ni/SiC (k = 10, 15 and 20 wt.%) as catalyst(s) at variable reaction temperatures, operated under Joule or Induction heating mode supplied as Supporting Information

References

1. Götz, M.; Lefebvre, J.; Mörs, F.; Koch, A. M.; Graf, F.; Bajohr, S.; R., R.; Kolb, T., Renewable Power-to-Gas: A technological and economic review. *Renew. Energ.* **2016**, *85*, 1371-1390.
2. Centi, G.; Quadrelli, E. A.; Perathoner, S., Catalysis for CO_2 conversion: a key technology for rapid introduction of renewable energy in the value chain of chemical industries. *Energy Environ. Sci.* **2013**, *6*, 1711-1731.
3. Hashimoto, K.; Kumagai, N.; Izumiya, K.; Takano, H.; Kato, Z., The Production of Renewable Energy in the Form of Methane Using Electrolytic Hydrogen Generation. *Energy Sustain. Soc.* **2014**, *4*, 17.
4. Jentsch, M.; Trost, T.; Sterner, M., Optimal Use of Power-to-Gas Energy Storage Systems in an 85% Renewable Energy Scenario. *Energy Procedia* **2014**, *46*, 254-261.
5. Rönsch, S.; Schneider, J.; Matthischke, S.; Schlüter, M.; Götz, M.; Lefebvre, J.; P., P.; Bajohr, S., Review on methanation-from fundamentals to current projects. *Fuel* **2016**, *166*, 276-296.
6. Wang, W.; Wang, S.; Ma, X.; Gong, J., Recent advances in catalytic hydrogenation of carbon dioxide. *Chem. Soc. Rev.* **2011**, *40*, 3703-3727.
7. Stankiewicz, A. I.; Moulijn, J. A., Process Intensification. *Ind. Eng. Chem. Res.* **2002**, *41*, 1920-1924.
8. Timko, B. P.; Whitehead, K.; Gao, W.; Kohane, D. S.; Farokhzad, O.; Anderson, D.; Langer, R., Advances in Drug Delivery. *Annu. Rev. Mater. Res.* **2011**, *41*, 1-20.
9. Norris, M. D.; Seidel, K.; Kirschning, A., Externally Induced Drug Release Systems with Magnetic Nanoparticle Carriers: An Emerging Field in Nanomedicine. *Adv. Therap.* **2019**, *2*, 1800092.
10. Hedayatnasab, Z.; Abnisa, F.; Wan Daud, W. M. A., Review on magnetic nanoparticles for magnetic nanofluid hyperthermia application. *Mater. Des.* **2017**, *123*, 174-196.

11. Lozinskii, M. G., *Industrial Applications of Induction Heating*. Pergamon: New York, NY, USA, 1969; p 690.
12. Wang, W.; Duong-Viet, C.; Xu, Z.; Ba, H.; Tuci, G.; Giambastiani, G.; Liu, Y.; Truong-Huu, T.; Nhut, J.-M.; Pham-Huu, C., CO_2 Methanation Under Dynamic Operational Mode Using Nickel Nanoparticles Decorated Carbon Felt (Ni/OCF) Combined with Inductive Heating. *Catal. Today* **2020**, *357*, 214-220.
13. Wang, W.; Duong-Viet, C.; Tuci, G.; Liu, Y.; Rossin, A.; Luconi, L.; Nhut, J.-M.; Nguyen-Dinh, L.; Giambastiani, G.; Pham-Huu, C., Highly Nickel-Loaded γ-Alumina Composites for a Radiofrequency-Heated, Low-Temperature CO_2 Methanation Scheme. *ChemSusChem* **2020**, *13*, 5468-5479.
14. Bordet, A.; Lacroix, L.-M.; Fazzini, P.-F.; Carrey, J.; Soulantica, K.; Chaudret, B., Magnetically Induced Continuous CO_2 Hydrogenation Using Composite Iron Carbide Nanoparticles of Exceptionally High Heating Power. *Angew. Chem. Int. Ed.* **2016**, *55*, 15894-15898.
15. De Masi, D.; Asensio, J. M.; Fazzini, P.-F.; Lacroix, L.-M.; Chaudret, B., Engineering Iron–Nickel Nanoparticles for Magnetically Induced CO_2 Methanation in Continuous Flow. *Angew. Chem. Int. Ed.* **2020**, *59*, 6187-6191.
16. Rivas-Murias, B.; Asensio, J. M.; Mille, N.; Rodríguez-González, B.; Fazzini, P.-F.; Carrey, J.; Chaudret, B.; Salgueiriño, V., Magnetically Induced CO_2 Methanation Using Exchange-Coupled Spinel Ferrites in Cuboctahedron-Shaped Nanocrystals. *Angew. Chem. Int. Ed.* **2020**, *59*, 15537-15542.
17. Niether, C.; Faure, S.; Bordet, A.; Deseure, J.; Chatenet, M.; Carrey, J.; Chaudret, B.; Rouet, A., Improved Water Electrolysis Using Magnetic Heating of FeC-Ni Core-Shell Nanoparticles. *Nat. Energy* **2018**, *3*, 476-783.

18. Díaz-Puerto, Z. J.; Raya-Barón, A.; van Leeuwen, P. W. N. M.; Asensio, J. M.; Chaudret, B., Determination of the surface temperature of magnetically heated nanoparticles using a catalytic approach. *Nanoscale* **2021**, *13*, 12438-12442.
19. Riedinger, A.; Guardia, P.; Curcio, A.; Garcia, M. A.; Cingolani, R.; Manna, L.; Pellegrino, T., Subnanometer local temperature probing and remotely controlled drug release based on azo-functionalized iron oxide nanoparticles. *Nano Lett.* **2013**, *13*, 2399-2406.
20. Meffre, A.; Mehdaoui, B.; Connord, V.; Carrey, J.; Fazzini, P. F.; Lachaize, S.; Respaud, M.; Chaudret, B., Complex Nano-objects Displaying Both Magnetic and Catalytic Properties: A Proof of Concept for Magnetically Induced Heterogeneous Catalysis. *Nano Lett.* **2015**, *15*, 3241-3248.
21. Hartman, T.; Geitenbeek, R. G.; Whiting, G. T.; Weckhuysen, B. M., Operando monitoring of temperature and active species at the single catalyst particle level. *Nat. Catal.* **2019**, *2*, 986-996.
22. Tuci, G.; Liu, Y.; Rossin, A.; Guo, X.-Y.; Pham, C.; Giambastiani, G.; Pham-Huu, C., Porous Silicon Carbide (SiC): a Chance for Improving Catalysts or just Another Active Phase Carrier? *Chem. Rev.* **2021**, *121*, 10559–10665.
23. O. Ersen; I. Florea; C. Hirlimann; Pham-Huu, C., Exploring nanomaterials with 3D electron microscopy. *Mater. Today* **2015**, *18*, 395-408.
24. I. Florea; O. Ersen; C. Hirlimann; L. Roiban; A. Deneuve; M. Houll; I. Janowska; P. Nguyen; C. Pham; Pham-Huu, C., Analytical electron tomography mapping of the SiC pore oxidation at the nanoscale. *Nanoscale* **2010**, *2*, 2668-2678.
25. P. Nguyen; Pham, C., Innovative porous SiC-based materials: From nanoscopic understandings to tunable carriers serving catalytic needs. *Appl. Catal. A, Gen.* **2011**, *391*, 443-454.

26. Toby, B. H.; Von Dreele, R. B., GSAS-II: the genesis of a modern open-source all purpose crystallography software package. *J. Appl. Cryst.* **2013**, *46*, 544-549.
27. For a standardized procedure see on "Datasheet & Manuals" at the following link: https://www.optris.global/optris-cslaser-lt (accessed October, 2021).
28. Cairns, R. W.; Ott, E., X-Ray Studies of the System Nickel—Oxygen—Water. I. Nickelous Oxide and Hydroxide. *J. Am. Chem. Soc.* **1933**, *55*, 527-533.
29. Jette, E. R.; Foote, F., Precision Determination of Lattice Constants. *J. Chem. Phys.* **1935**, *3*, 605-616.
30. Jenkins, R.; Snyder, R. L., Introduction to X-ray Powder Diffractometry. John Wiley & Sons Inc.: 1996; pp 89-91.
31. Liu, Y.; Edouard, D.; Nguyen, L. D.; Begin, D.; Nguyen, P.; Pham, C.; Pham-Huu, C., High Performance Structured Platelet Milli-Reactor Filled with Supported Cobalt Open Cell SiC Foam Catalyst for the Fischer-Tropsch Synthesis. *Chem. Eng. J.* **2013**, *222*, 265-273.
32. Nesbitt, H. W.; Legrand, D.; Bancroft, G. M., Interpretation of Ni2p XPS spectra of Ni conductors and Ni insulators. *Phys. Chem. Minerals* **2000**, *27*, 357-366.
33. Liu, B.; Liu, L. R.; Liu, X. J.; Liu, M. J.; Xiao, Y. S., Variation of crystal structure in nickel nanoparticles filled in carbon nanotubes. *Mater. Sci. Technol.* **2012**, *28*, 1345-1348.
34. Lin, Y.-R.; Ho, C.-Y.; Chuang, W.-T.; Ku, C.-S.; Kai, J.-J., Swelling of ion-irradiated 3C–SiC characterized by synchrotronradiation based XRD and TEM. *J. Nucl. Mater.* **2014**, *455*, 292-296.
35. Pujula, M.; Sanchez-Rodriguez, D.; Lopez-Olmedo, J. P.; Farjas, J.; Roura, P., Measuring thermal conductivity of powders with differential scanning calorimetry. *J. Therm. Anal. Calorim.* **2016**, *125*, 571-577.

36. Chen, D.-X.; Pascu, O.; Roig, A.; Sanchez, A., Size analysis and magnetic structure of nickel nanoparticles. *J. Magn. Magn.* **2010**, *322*, 3834-3840.

37. He, X.; Zhong, W.; Au, C.-T.; Du, Y., Size dependence of the magnetic properties of Ni nanoparticles prepared by thermal decomposition method. *Nanoscale Res. Lett.* **2013**, *8*, 446 (10).

38. Li, L.; Zheng, J.; Liu, Y.; Wang, W.; Huang, Q.; Chu, W., Impacts of SiC Carrier and Nickel Precursor of NiLa/support Catalysts for CO_2 Selective Hydrogenation to Synthetic Natural Gas (SNG). *ChemistrySelect* **2017**, *2*, 3750-3757.

39. Vrijburg, W. L.; Moioli, E.; Chen, W.; Zhang, M.; Terlingen, B. J. P.; Zijlstra, B.; Filot, I. A. W.; Züttel, A.; Pidko, E. A.; Hensen, E. J. M., Efficient base-metal NiMn/TiO_2 catalyst for CO_2 methanation. *ACS Catal.* **2019**, *9*, 7823-7839.

40. Xu, L.; Wang, F.; Chen, M.; Nie, D.; Lian, X.; Lu, Z.; Chen, H.; Zhang, K.; Ge, P., CO_2 methanation over rare earth doped Ni based mesoporous catalysts with intensified low-temperature activity. *Int. J. Hydrog. Energy* **2017**, *42*, 15523-15539.

41. Asensio, J. M.; Miguel, A. B.; Fazzini, P.-F.; van Leeuwen, P. W. N. M.; Chaudret, B., Hydrodeoxygenation Using Magnetic Induction: High-Temperature Heterogeneous Catalysis in Solution. *Angew. Chem. Int. Ed.* **2019**, *58*, 11306-11310.

42. Niether, C.; Faure, S.; Bordet, A.; Deseure, J.; Chatenet, M.; Carrey, J.; Chaudret, B.; Rouet, A.; Nat. Energy 3, Improved water electrolysis using magnetic heating of FeC–Ni core–shell nanoparticles. *Nat. Energy* **2018**, *3*, 476 (8).

43. Périgo, E. A.; Hemery, G.; Sandre, O.; Ortega, D.; Garaio, E.; Plazaola, F.; Teran, F. J., Fundamentals and advances in magnetic hyperthermia. *Appl. Phys. Rev.* **2015**, *2*, 041302 (35).

44. Díaz-Puerto, Z. J.; Raya-Barón, A.; van Leeuwen, P. W. N. M.; Asensio, J. M.; Chaudret, B., Determination of the surface temperature of magnetically heated nanoparticles using a catalytic approach. *Nanoscale* **2021**, DOI: 10.1039/D1NR02283K.

45. Bordet, A.; Lacroix, L.-M.; Fazzini, P. F.; Carrey, J.; Soulantica, K.; Chaudret, B., Magnetically Induced Continuous CO_2 Hydrogenation Using Composite Iron Carbide Nanoparticles of Exceptionally High Heating Power. *Angew. Chem. Int. Ed.* **2016**, *55*, 15894-15898.

46. Julian, I.; Ramirez, H.; Hueso, J. L.; Mallada, R.; Santamaria, J., Non-oxidative methane conversion in microwave-assisted structured reactors. *Chem. Eng. J.* **2019**, *377*, 119764 (12).

47. Ramirez, A.; Hueso, J. L.; Mallada, R.; Santamaria, J., In situ temperature measurements in microwave-heated gas-solid catalytic systems. Detection of hot spots and solid-fluid temperature gradients in the ethylene epoxidation reaction. *Chem. Eng. J.* **2017**, *316*, 50-60.

48. Pearce, J.; Giustini, A.; Stigliano, R.; Hoopes, P. J., Magnetic Heating of Nanoparticles: The Importance of Particle Clustering to Achieve Therapeutic Temperatures. *J. Nanotechnol. Eng. Med.* **2013**, *4*, 0110071–01100714.

49. Moses, A. J., Eddy current losses in soft magnetic materials. In *Wiley Encyclopedia of Electrical and Electronics Engineering*, Wiley: 2016; pp 1-22.

50. Appino, C.; De La Barrière, O.; Fiorillo, F.; Lobue, M.; Mazaleyrat, F.; Ragusa, C., Classical eddy current losses in Soft Magnetic Composites. *J. Appl. Phys.* **2013**, *113*, 17A322-1-17A322-3.

51. Ruta, S.; Chantrell, R.; Hovorka, O., Unified model of hyperthermia via hysteresis heating in systems of interacting magnetic nanoparticles. *Sci. Rep.* **2015**, *5*, 9090.

52. Hergt, R.; Dutz, S.; Röder, M., Effects of size distribution on hysteresis losses of magnetic nanoparticles for hyperthermia. *J. Phys. Condens. Matter.* **2008**, *20*, 385214.
53. Kuz'min, M. D., Shape of Temperature Dependence of Spontaneous Magnetization of Ferromagnets: Quantitative Analysis. *Phys. Rev. Lett.* **2005**, *94*, 107204 (4).
54. Crangle, J.; Goodman, G. M., The Magnetization of pure iron and nickel. *Proc. R. Soc. London A* **1971**, *321*, 477 (15).
55. Carrey, J.; Mehdaoui, B.; Respaud, M., Simple Models for Dynamic Hysteresis Loop Calculations of Magnetic Single-Domain Nanoparticles: Application to Magnetic Hyperthermia Optimization. *J. Appl. Phys.* **2011**, *109*, 083921 (17).
56. Houlding, T. K.; Rebrov, E. V., Application of Alternative Energy Forms in Catalytic Reactor Engineering. *Green Process Synth.* **2012**, *1*, 19-31.
57. Sechovský, V., In *In Encyclopedia of Materials: Science and Technology*, Buschow, K. H. J.; Cahn, R. W.; Flemings, M. C.; Ilschner, B.; Kramer, E. J.; Mahajan, S.; Veyssière, P., Eds. Elsevier: Amsterdam, 2001; p 5021.
58. Frederikse, H. P. R., In *Handbook of Chemistry and Physics; Properties of magnetic materials*, CRC Press LLC: Boca Raton, FL, 2009.

For Table of Contents Use Only

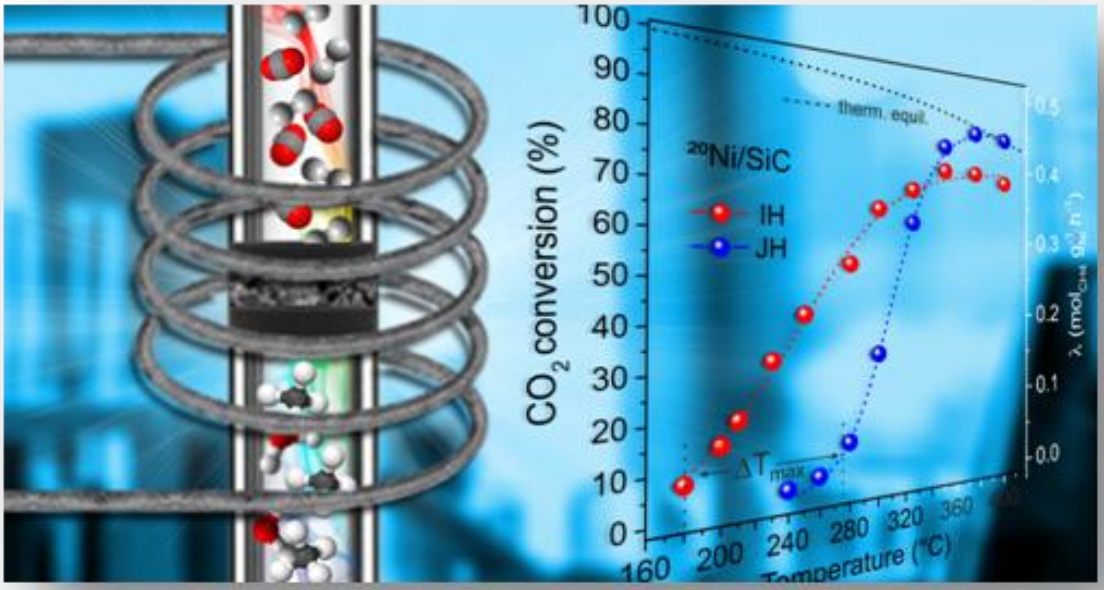

Sabatier reaction operated under two distinct heating configurations has offered a practical tool to map the real temperature of radiofrequency excited metal nano-objects engaged in the catalytic process.